Advanced Composites and Hybrid Materials (2022) 5:3035–3044
https://doi.org/10.1007/s42114-022-00549-5

ORIGINAL RESEARCH

Efficient photothermal deicing employing superhydrophobic plasmonic MXene composites

Jiaying Wang[1] · Peihang Li[1] · Peng Yu[2] · Tim Leydecker[1] · Ilker S. Bayer[3] · Dusan Losic[4] · Arup Neogi[1] · Zhiming Wang[1,5]

Received: 26 April 2022 / Revised: 27 July 2022 / Accepted: 18 August 2022 / Published online: 9 September 2022

Abstract

Deicing and anti-icing on the surface, such as train tracks, highways, airports, aircraft, cars, ships, wind turbines, and outdoor cables, represent a significant challenge. Many different chemical compounds and coatings were explored and used to address these problems, but some limitations remain. The anti-icing ability under low temperature and high humidity conditions, the low deicing efficiency, and the complex preparation method, etc., restrict the application and development of deicing materials. This paper presents a simple and efficient solution based on new plasmonic photothermal superhydrophobic composite coatings. A hybrid MXene@Au-waterborne polyurethane (MXene@Au-WPU) coating is specifically designed to realize a significant temperature rise due to the high absorption and rapid heat transfer of the plasmonic MXene@Au in the entire coating. To achieve superhydrophobicity, chemically modified SiO_2 nanoparticles were deposited on the surface of the MXene@Au-WPU layer to obtain a fSiO_2/MXene@Au-WPU(fluoroalkyl silanes-SiO_2/MXene@Au-WPU) superhydrophobic photothermal coating featuring a contact angle of 153°. The composite coating was demonstrated to be adequate for anti-icing and deicing applications, with an ultra-long anti-icing time of 1053 s under low temperature and high humidity conditions (− 20 °C, relative humidity 68%). Compared to previous work, the coating also achieved a super high photothermal deicing efficiency of 73.1%. The result presented in the article furthermore demonstrates resistance to corrosive liquids with pH ranging from 1 to 13. A combination of the anti-icing, corrosion-resistance, and facile implementation features of this multifunctional coating enhances its high potential for implementation in various surface technologies.

Keywords Photothermal deicing · Superhydrophobic · MXene · Plasmonic · Composite coating

1 Introduction

The design and fabrication of reliable and large-scale adaptable non-wetting photothermal coatings with anti-icing/deicing properties are increasingly becoming central in surface science and technology as the ice formation and accumulation can cause critical damage to various energy transport and conversion systems such as power lines [1], aircraft engines [2], and wind turbines [3]. Well-established active deicing methods include electric heating [4], chemical treatment targeting freezing point suppression [5], and mechanical deicing. However, these technologies have disadvantages and limitations, such as being energy-intensive and low-efficiency [6, 7]. Hence, passive anti-icing materials technologies have been developed rapidly to address some of these limitations [8–11]. Passive anti-icing materials aim to either delay or suppress the formation of ice droplets and crystals, minimize the

✉ Arup Neogi
arup@uestc.edu.cn

✉ Zhiming Wang
zhmwang@uestc.edu.cn

1 Institute of Fundamental and Frontier Sciences, University of Electronic Science and Technology of China, Chengdu 610054, China

2 College of Optoelectronic Technology, Chengdu University of Information Technology, Chengdu 610225, China

3 Smart Materials, Istituto Italiano di Tecnologia, Via Morego 30, 16163 Genova, Italy

4 School of Chemical Engineering and Advanced Materials, The University of Adelaide, Adelaide, SA 5005, Australia

5 Institute for Advanced Study, Chengdu University, Chengdu 610106, China

adhesion strength of the ice, or ideally be capable of both simultaneously. Non-wetting coatings with photothermal energy harnessing properties are ideal candidates for photothermal deicing applications [7, 8, 12–17].

In developing these new passive anti-icing coatings, it is also important to improve their photothermal superhydrophobic properties through low-cost, easily achievable processes such as spray or dip coating. The spray coating of superhydrophobic suspensions or inks is increasingly chosen as a go-to approach to synthesizing multifunctional superhydrophobic coatings [18–21]. A coating can gain superhydrophobic properties by the surface-grafting of nanostructures containing superhydrophobic functional groups. Zhang et al., for instance, sprayed a waterborne polyurethane solution and modified SiO_2 nanoparticles (NPs) successively to transform metal, silicon wafer, and polymer film surfaces into non-wetting nanostructures [22]. However, coating obtained through the grafting of superhydrophobic chemical moieties on functional nanomaterials should maintain their functionality, such as photothermal response in order to fabricate multifunctional superhydrophobic coatings. For harnessing photothermal energy, the functional nanomaterial must display an efficient light-to-heat conversion effect within the coating.

The actual performance of superhydrophobic photothermal coatings is dependent on the optical properties, thermal conductivity, and dispersion state of the fillers. An optimized design of nanomaterials and nanostructures can facilitate high energy absorption with ideal optical properties [23, 24] for enhancing efficient heat generation [25–28]. MXene($Ti_3C_2T_x$) features a localized surface plasmon (LSPR) enhancement effect and a broad absorption band [29–31]. Moreover, because MXenes have good electrical conductivity, they can be used in flexible electronic devices and soft robots [32, 33]. When used as plasmonic metamaterials, MXenes can be employed as electromagnetic shielding materials [34–36]. Due to its superior optical properties and fast heat transfer capabilities, MXene has been widely used in light absorption and light-to-heat conversion devices [29, 31, 37, 38]. To further enhance the photothermal performance of MXene, researchers have hybridized it with Au or Ag NPs. While previous works have demonstrated the hybrid MXene@Au NPs could synergistically improve light absorption and heat generation of the photothermal performance [39–41], there are few reports on the use of MXene@Au hybrids in superhydrophobic photothermal films. It is due to the fact that non-aqueous systems usually used in the preparation of superhydrophobic films result in the coagulation of Au NPs, restricting the photothermal performance of this hybrid material.

A new strategy is proposed to develop efficient photothermal deicing coatings employing superhydrophobic plasmonic MXene composites. A two-step spraying process was employed to prepare plasmonic photothermal superhydrophobic coatings containing MXene@Au hybrids combined with waterborne polyurethane. Modified SiO_2 NPs with fluoroalkyl silane (FAS) moieties were deposited on the coating's surface to fabricate $fSiO_2$/MXene@Au-WPU photothermal superhydrophobic coatings. The prepared $fSiO_2$/MXene@Au-WPU composite coating is successfully explored and can be applied for anti-icing and deicing over an ultra-long anti-icing time under low temperature and high humidity. The strategy for preparing multifunctional superhydrophobic photothermal composite coatings proposed in this work is simple, efficient, and easy to operate under various conditions with broad practical applications. This multifunctional coating can be easily implemented for photothermal deicing and corrosion-resistant coating for various surface protection technologies.

2 Experimental section

The synthesis route of the plasmonic-enhanced superhydrophobic MXene composite film is explained in Fig. 1a. The diagram of the deicing process of this composite coating is shown in Fig. 1b. Layered MXene was etched from MAX(Ti_3AlC_2) using a conventional chemical etching process [42, 43]. Au NPs were synthesized by the seed-mediated growth method [44]. MXene nanosheets were combined with Au NPs to create plasmonic hybrid structures of MXene@Au, using ultrasonic stirring with the help of their electrostatic interaction. MXene@Au powders were then dispersed into the WPU matrix.

The $fSiO_2$ was prepared by chemical grafting of FAS on SiO_2 particles following recipes well-established in the literature [45, 46]. The modified $fSiO_2$ layer was subsequently sprayed on the MXene@Au-WPU film. Figure 1b illustrates the ice melting mechanism of the superhydrophobic photothermal coating. The detailed experimental procedure and synthesis process of prepared materials and their characterizations using scanning electron microscopy (SEM), transmission electron microscopy (TEM), X-ray diffraction spectroscopy (XRD), energy-dispersive X-ray spectroscopy (EDS), and X-ray photoelectron spectroscopy (XPS) measurements are described in the Supporting Information.

3 Results and discussion

The structural properties of the fabricated MXene nanosheets and MXene@Au hybrids were investigated using SEM and TEM (Fig. 2). Multilayered MXene sheets structures can be observed from the cross-section of the SEM images (Fig. 2b). The gaps between the MXene layer provide host

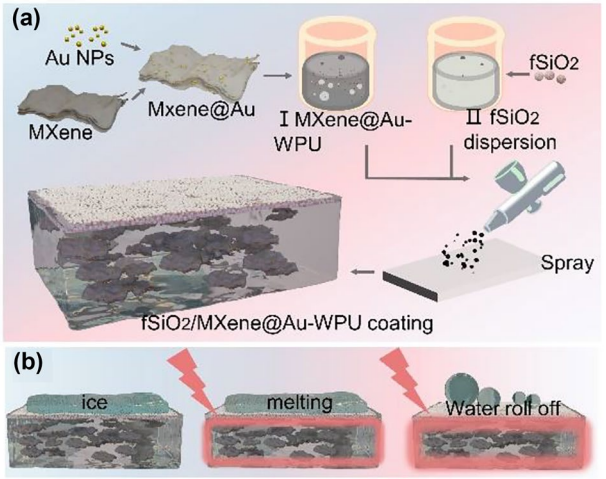

Fig. 1 **a** Schematic diagram of the fabrication of the $fSiO_2$/MXene@Au-WPU composite film. **b** Schematic diagram of the deicing process of $fSiO_2$/MXene@Au-WPU superhydrophobic photothermal coatings

sites to embed additional nanomaterials or serve as compounding sites [40, 47]. The synthesis of MXene from the MAX material is further confirmed by XRD, as shown in Fig. S1a [29, 30].

The MXene nanosheets were added to WPU, and the MXene-WPU coating was formed after spraying. Figure S1b showed the absorption spectrums of coatings when the mass ratio of MXene in MXene-WPU was optimized to 3%. The absorption peak observed at 800 nm can be attributed to the LSPR of the plasmonic MXene nanosheets [29–31].

Figure S2a shows the morphologies of the as-prepared gold nanoparticles with diameters ranging from 25 to 35 nm. Figure 2c–d show that Au NPs were successfully infiltrated within the layered MXene, yielding MXene@Au composite structures. The TEM image in Fig. 2e demonstrates the MXene@Au structure, consistent with the SEM characterization showing that the Au NPs are distributed on the flake-shaped MXene. High-resolution TEM was performed on the hybrid structure (Fig. S2b), and revealed that the interplanar distance corresponds to the (111) crystal plane of metallic Au [48, 49]. EDS mapping of Ti, C, and Au shows the corresponding results in Fig. 2f.

The material compositions were investigated using XRD and XPS (Fig. 3). XRD patterns of MXene and MXene@Au depicted in Fig. 3a feature peaks at 38.4°, 44.6°, and 64.8°, which can be attributed to the crystallographic planes of the metallic gold [39]. The hybrid structure was further characterized by XPS, and as can be seen in Fig. 3b, XPS results demonstrate the successful hybridization of metallic gold onto MXene nanosheets since the peaks of Au 4f and Au 4d could be observed. The main elements of MXene, Ti, and C were detected in the MXene@Au spectrum. Since there are fluorine-containing and oxygen-containing functional groups on the MXene layers, the peaks of O and F appear in the spectrum [31, 50, 51]. Figure 3c and d show high-resolution XPS spectra of Ti 2p and C 1 s in MXene@Au hybrids. The chemical bond information featured in Fig. S3 indicates that Ti-C, Ti–O, and Ti(III) accounted for 15.3%, 13.5%, and 40.3% in the spectrum of Ti 2p, respectively. C–C, C-Ti, and C-O bonds account for 64.8%, 16.1%, and 5.2%, respectively, in the spectrum of C 1 s. These further confirmed the $Ti_3C_2T_x$ composition in the hybrid structure [41, 52, 53]. In Fig. 3e and f, there are diffraction peaks in Au 4f and Au 4d core-level XPS spectrum, respectively [54, 55]. The Au 4f spectrum contains two diffraction peaks; the peaks at 83.6 eV and 87.2 eV are related to the binding energies of Au $4f_{7/2}$ and Au $4f_{5/2}$, respectively [52]. The peaks at 334.3 eV and 352.6 eV correspond to Au $4d_{5/2}$ and Au $4d_{3/2}$, respectively [56]. Au exists in a metallic state in the hybrid rather than forming chemical bonds with other elements.

SEM, TEM, XRD, and XPS characterizations confirm that Au NPs are successfully hybridized with MXene nanosheets and form the MXene@Au composite material. When the mass ratio of MXene is fixed (3%), the

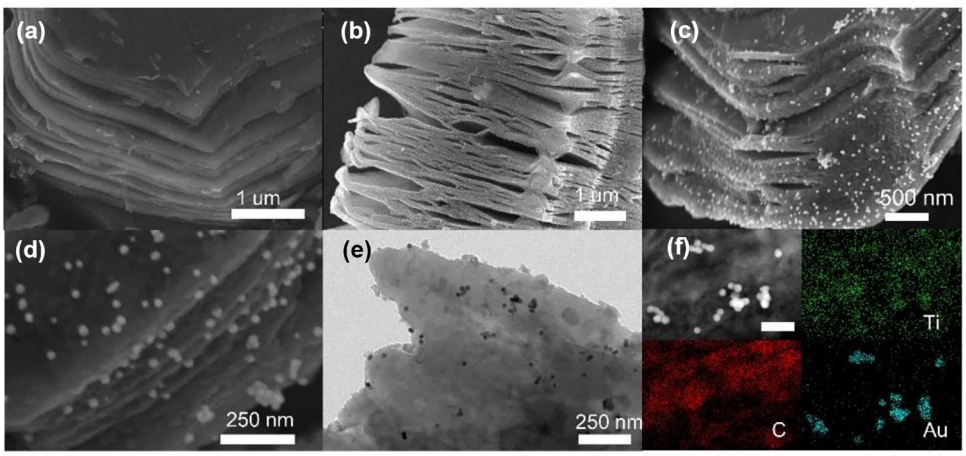

Fig. 2 **a–b** SEM images of the MXene nanosheets. **c–d** SEM images of the MXene@Au hybrid nanomaterial. **e** Low-resolution TEM image of the MXene@Au hybrid nanomaterial. **f** EDS elemental mapping images of Ti, C, and Au for the MXene@Au hybrid, and the scale bar corresponds to 100 nm

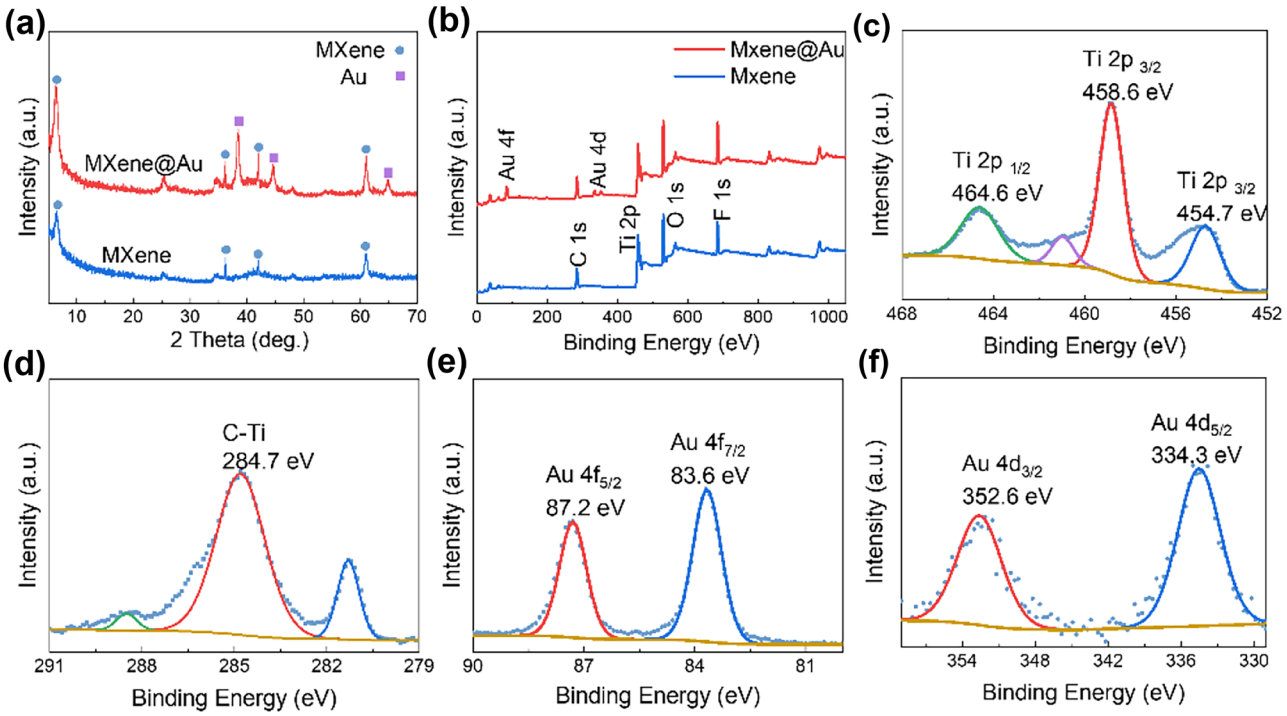

Fig. 3 **a** XRD patterns for pure MXene nanosheets and the MXene@Au hybrid. **b** XPS spectrums of the pure MXene nanosheets and the MXene@Au hybrid. **c**–**f** High-resolution XPS spectrums of Ti 2p, C 1 s, Au 4f, and Au 4d for the MXene@Au hybrid nanomaterial

optimal ratio for MXene to Au is 8:1, as shown in Fig. S2c. In Fig. 4a, the absorption of MXene@Au-WPU film is higher than that of MXene-WPU, which indicates that the hybridized MXene@Au nanocomposite has better optical properties. The inset picture shows the ultraviolet – visible (UV–VIS) spectrometry of MXene and MXene@Au solution. The NIR absorption peak (~ 800 nm) of the MXene nanosheets can be observed, consistent with the previously reported plasmonic peak of MXene [29–31]. After hybridizing with Au NPs, the absorption of MXene is enhanced in NIR. The absorption peak around 550 nm is due to the LSPR of Au NPs [39, 41]. The MXene@Au-WPU layer inherits the absorption band of the hybridization nanomaterials in NIR. Multiple previous reports are focused on MXene-based photothermal materials using NIR irradiation light sources [41, 57–60]. NIR light sources for heating and deicing also have important research value in many applications [12, 13, 15, 16]. Hence, the experimental characterization of the light-to-heat transfer in the samples was performed at 808 nm irradiation.

The MXene-WPU and MXene@Au-WPU composite films were exposed to different power densities, as shown in Fig. 4b–c. The surface temperature of pure WPU is shown in Fig. S4. WPU had a relatively minor contribution to the photothermal conversion, and the photothermal properties of the film are mainly attributed to the added filler, MXene@Au hybrid. The surface temperatures of the MXene-WPU and the MXene@Au-WPU film increased with the irradiation time and reached equilibrium values around 300 s. Under the same power density of laser irradiation, the overall temperature of MXene@Au-WPU was higher than that of MXene-WPU. The equilibrium temperature of MXene@Au-WPU film at 0.5 W cm^{-2} was 130.2 °C, while the MXene-WPU film approached 110.3 °C.

The differences in the temperature increase of MXene-WPU and MXene@Au-WPU films under lasers of different powers are shown in Fig. 4d. As shown in Fig. 4e. the surface equilibrium temperatures of the MXene@Au-WPU hybrid the film did not decrease after multiple irradiations with different powers, indicating good repeatability and no fatigue photothermal effect [51]. Figure 4f shows the IR images of MXene-WPU and MXene@Au-WPU coatings as a function of time. The region representing the high-temperature diffusion on the hybrid film is larger than that of the unhybridized film. Compared to one particular heat-generating property in the MXene-WPU film, the photothermal ability of the MXene@Au-WPU can be attributed to the synergistic effect of MXene nanosheets and Au NPs [39, 41]. The hydrophilic functional groups on the MXene nanosheets facilitate uniform dispersion of the MXene@Au hybrid in WPU and thus contribute to the homogenous thermal conduction in the entire film [61]. The addition of Au NPs also gives the hybrid structure higher absorption and photothermal performance [39, 41].

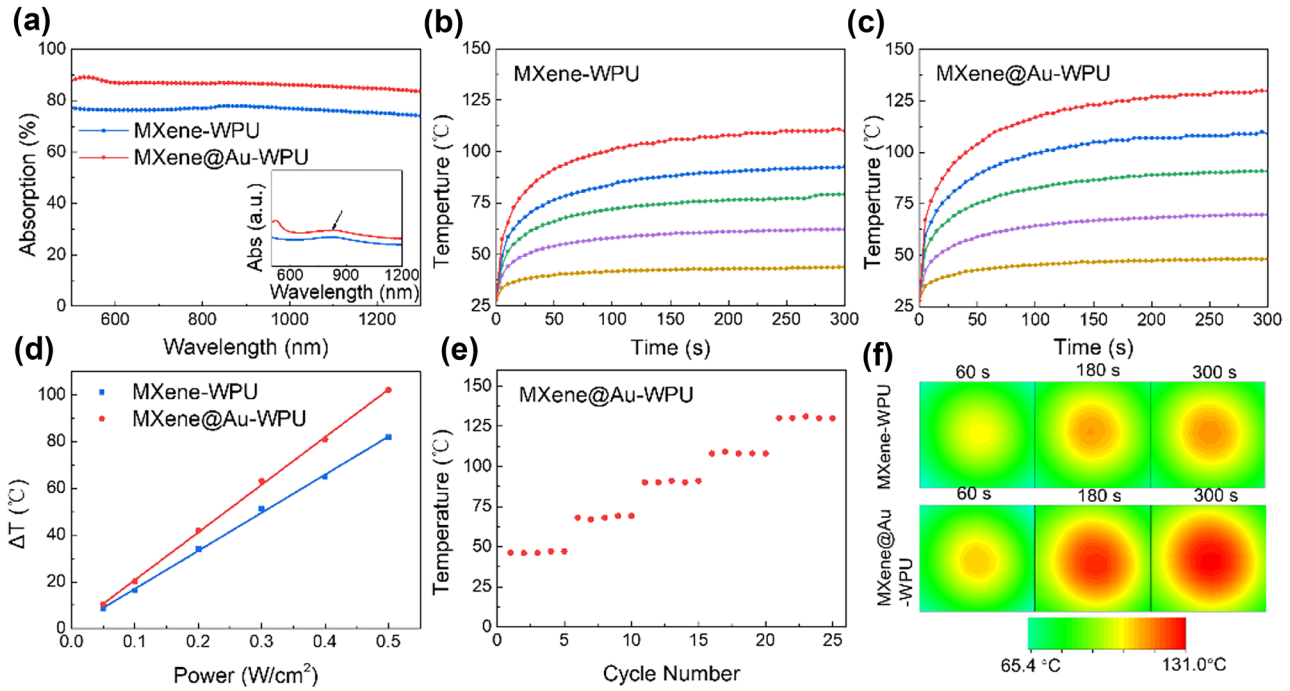

Fig. 4 **a** Absorption spectrums of the composite coating. The inset is a UV–VIS measurement of the MXene@Au solution (red) and the MXene solution (blue). **b**, **c** The photothermal-heating curves of the composite coatings at different power (0.1, 0.2, 0.3, 0.4, and 0.5 W cm^{-2}). **d** Temperature increase (ΔT) as functions of the irradiated power density for the composite coatings after an irradiation time of 300 s. **e** Photothermal stability of the MXene@Au-WPU composite coating at five optical power densities (0.1, 0.2, 0.3, 0.4, and 0.5 W cm^{-2}) for twenty-five cycles. In each cycle, the stable film surface temperature was recorded at 300 s. **f** IR thermal images of the composite coatings at 0.5 W cm^{-2}

These indicate that the hybrid material has better optical performance, heat transfer conductivity, and photothermal conversion ability. In depth analysis if the hybrid materials at the microscopic scale and study of the thermal conduction dynamics of the materials will be the focus of subsequent work endeavors. Notably, the films' optical and thermal characterizations demonstrate the bright potential of the prepared hybrid materials as photothermal coatings.

A superhydrophobic SiO_2 layer was introduced to modify the surface of the composite coating to improve its hydrophobicity and make it more suitable for deicing applications. The SiO_2 NPs were prepared by the Stober method. The SEM image of the morphology (Fig. S5a) [62] revealed that the SiO_2 nanoparticles were spherical, ranging from 150 to 170 nm in diameter. FAS, a chemical reagent typically used to improve hydrophobicity, was thoroughly mixed and reacted with SiO_2 NPs. FAS-SiO_2 NPs were obtained after heat-drying. The chemical treatment on the surface did not change the morphology of SiO_2 NPs, as shown in Fig. 5a. The XPS characterization was performed on FAS-SiO_2 and SiO_2 (Fig. S5b). Compared with the spectrum of SiO_2, the F 1 s peak of FAS-SiO_2 was much higher, indicating that the fluorinated functional groups in FAS were grafted on the SiO_2 NPs [45, 46].

After spraying the FAS-SiO_2 solution on the surface of the MXene@Au-WPU films, a multifunctional composite coating was obtained. In Fig. 5b, the cross-section image shows that the FAS-SiO_2 layer connected by the NPs clusters was closely attached to the surface of the MXene@Au-WPU composite coating to form the fSiO_2/MXene@Au-WPU composite coating. The contact angle (CA) measurement of MXene@Au-WPU, SiO_2/MXene@Au-WPU, and fSiO_2/MXene@Au-WPU composite coatings are shown in Fig. 5c1, c2, and c3, respectively. Therefore, the MXene@Au-WPU film was hydrophilic [63], closely related to the hydrophilicity of MXene nanosheets and the WPU polymer. On the other hand, the SiO_2/MXene@Au-WPU film was hydrophobic, while the fSiO_2/MXene@Au-WPU film was superhydrophobic [63–66]. A sliding angle (SA) value of 4.5°, indicating the superhydrophobicity of fSiO_2/MXene@Au-WPU film, was measured [7, 65]. The composite film with SiO_2 NPs featured undulating spherical protrusions, similar to the lotus leaf structure in bionics.

It significantly reduces the wettability of water droplets, making the film sprayed with SiO_2 coating change from hydrophilic to hydrophobic [63, 65]. Additionally, the surface of the modified SiO_2 spheres was grafted with hydrophobic functional groups, reducing the surface tension and

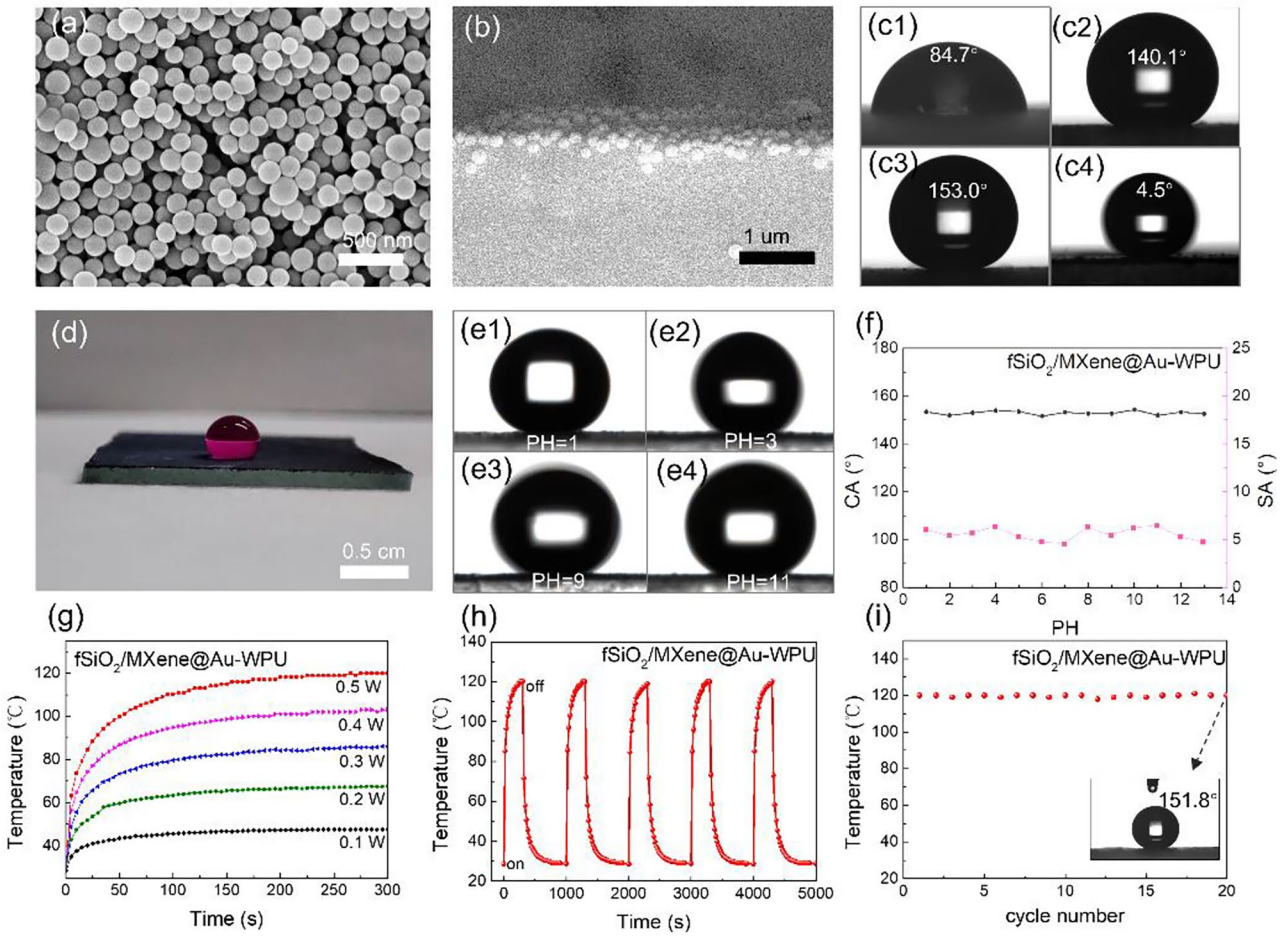

Fig. 5 **a** SEM image of the modified FAS-SiO_2 NPs. **b** SEM image of the $fSiO_2$/MXene@Au-WPU composite film (cross-section). **c1**–**c3** CA characterizations of MXene@Au-WPU, SiO_2/MXene@Au-WPU, and $fSiO_2$/MXene@Au-WPU composite coatings. **c4** SA characterization of $fSiO_2$/MXene@Au-WPU composite film. **d** The photograph shows the water droplets formed by the rhodamine B solution on the $fSiO_2$/MXene@Au-WPU coating. **e** Optical images of static water droplets of different pH values on the $fSiO_2$/MXene@Au-WPU coating. **f** CA and SA for solutions with pH from 1 to 13. **g** The photothermal-heating curves of the $fSiO_2$/MXene@Au-WPU coating. **h** Heating curves for five lasers on/off cycles at 0.5 W cm^{-2}. **i** Photothermal stability of the $fSiO_2$/MXene@Au-WPU composite coating for twenty cycles at 0.5 W cm^{-2}. The inset is the optical image of water droplets on the coating after cycles

further enhancing the hydrophobicity of the film, making the $fSiO_2$/MXene@Au-WPU coating possess superhydrophobic properties [67, 68]. We optimized the F-SiO_2 content on the surface of the composite films. Different layers of F-SiO_2 nanoparticles were sprayed on the films, and their absorption spectra and contact angles were characterized. In every layer sprayed, 5 mg of F-SiO_2 nanoparticles were sprayed on the film surface. From Fig. S6, CA increased when more F-SiO_2 nanoparticles were sprayed, while the absorption decreased. The scattering of incident light by SiO_2 reduced the absorption of light. However, when the coverage density of F-SiO_2 particles is increased, the hydrophilic area is reduced, and the superhydrophobic area on the surface of the composite film is increased. F3 was chosen as the optimized formulation since the $fSiO_2$/Mxene@Au-WPU film with three F-SiO_2 sprayed layers provided the most optimum performance for absorption and superhydrophobicity. Unless otherwise specified, $fSiO_2$/Mxene@Au-WPU composite films used in this work were synthesized with this formulation.

Figure 5d is a photograph showing the perfect water droplet on the superhydrophobic $fSiO_2$/MXene@Au-WPU coating. The water droplet in the photo uses red dye to make it look clearer. In addition, the superhydrophobic coating was proven to withstand both concentrated acid and alkali solutions, as shown in Fig. 5e and f, where the coatings exhibited superhydrophobic properties for solutions with a pH ranging from 1 to 13.

A similar thermal radiation heating treatment is applied to evaluate the performance of the superhydrophobic $fSiO_2$/MXene@Au-WPU composite coating. Figure 5g shows the effect of photothermal radiation with increasing power

density. Similar to the MXene@Au-WPU coating, the temperature difference of the $fSiO_2$/MA-WPU coating shows a positive correlation with the power density of the irradiation. The temperature reached 120 °C when irradiated with a power density of 0.5 W cm^{-2}. Although the absorption of $fSiO_2$/MXene@Au-WPU was slightly lower than that of the MXene@Au-WPU film (Fig. S7), the composite coating still reached high temperature under mild irradiation, achieving good light-to-heat conversion efficiency. Due to the high optical bandgap of SiO_2 and its transparency, the MXene@Au hybrid structure can rapidly absorb the light energy and promotes uniform heating of the entire coating. Repeated thermal cycles were carried out to characterize the photothermal stability of the $fSiO_2$/MXene@Au-WPU composite coating, as shown in Fig. 5h and i. In the five processes of irradiating on and off, the temperature curve of the coating was similar, with little difference in the maximum temperature of light-to-heat conversion after twenty heating cycles. It indicates that the $fSiO_2$/MXene@Au-WPU films offer good repeatability and exhibit no fatigue due to the photothermal effect. The CA and SA after cycling heating are shown in Fig. 5i (inset) and Fig. S8, demonstrating that the superhydrophobic properties also remain stable upon cycling.

As an actual application of the photothermal superhydrophobic coating, the anti-icing and deicing performances of the coatings were measured. The coatings were placed on a cold platform maintained at − 20 °C. As shown in Fig. 6a and Movie S1, the time for the water droplet (20 µL) to freeze on the $fSiO_2$/MXene@Au-WPU coating was five times longer than on the MXene@Au-WPU coating (1053 s vs. 212 s), due to the narrow air gaps between the water and the superhydrophobic coating, slowing down the freezing process. The water-droplet could be maintained above the freezing temperature for a long time, thereby inhibiting the formation of ice [8, 12]. Compared with previous reports (Table 1), the superhydrophobic coating we prepared featured an ultra-long anti-icing time under low temperature and high humidity [12–17].

Figure 6b (Movie S2) shows that the superhydrophobic $fSiO_2$/MXene@Au-WPU coating developed a good frost resistance, as the anti-frosting time was improved by 1.6 times compared to the MXene@Au-WPU coating. The defrosting performance is shown in Fig. S9 and Movie S3. The tiny water droplets on the superhydrophobic fSiO2/MXene@Au-WPU film surface are not easy to aggregate, inhibiting the frost layer formation [69]. As the frost melts, the melting area of the frost on the $fSiO_2$/MXene@Au-WPU coating is 3.4 times that of the MXene@Au-WPU coating.

The deicing performance of the coatings was next characterized, as shown in Fig. 6c and Movie S4. The ice discs (diameter, 2 cm) with a thickness of 3 mm on the sample were irradiated. The ice on the $fSiO_2$/MXene@Au-WPU coating melted completely in 60 s, while the ice on the MXene@Au-WPU melted by 32%. Furthermore, the $fSiO_2$/MXene@Au-WPU coating reached a higher temperature under the deicing irradiation than the non-modified coatings (28.9 °C vs. 20.2 °C). After the light penetrates the hydrophobic $fSiO_2$ layer, the MXene@Au hybrids quickly and effectively conduct light-to-heat conversion and uniformly transfer the heat to the entire film. Due to the superhydrophobic properties of the coating, the water produced by the ice-melting slips away from the surface. The specific heat capacity of air is less than that of water, so the dry area on $fSiO_2$/MXene@Au-WPU coating dissipates heat faster than the wet area on MXene@Au-WPU coating during the melting process, which is

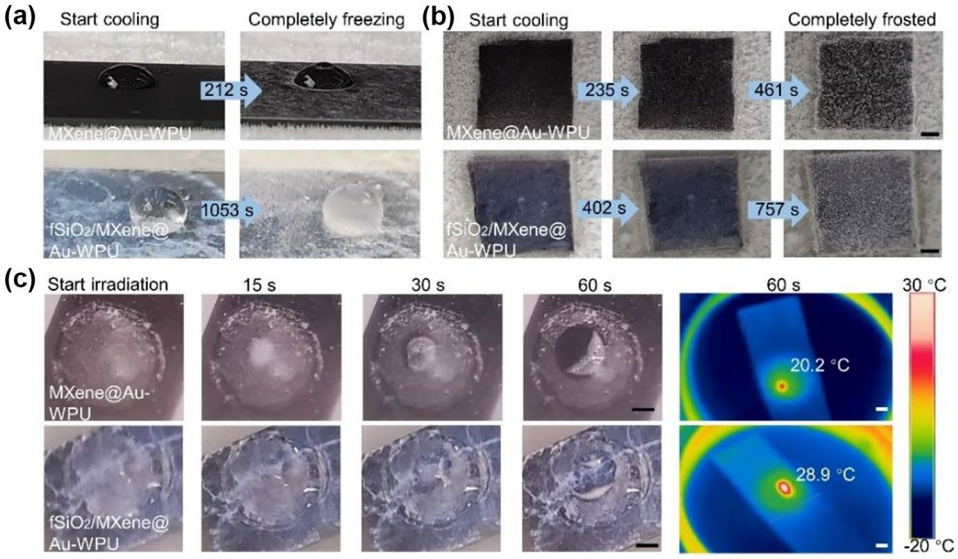

Fig. 6 **a**–**b** Photographs of the freezing and frosting processes on MXene@Au-WPU coating and $fSiO_2$/MXene@Au-WPU coating. **c** Pictures of the photothermal deicing process of MXene@Au-WPU coating

Table 1 Anti-icing and deicing performances among published literature and this work

Temperature of cold panel/°C	Relative humidity (RH)/%	Time of anti-icing/s	Power of deicing laser (808 nm)/W cm^{-2}	Efficiency of deicing/%	Ref
− 20	30	165	1	-	[13]
− 20	30	480	1	-	[16]
− 10	65	78	1	-	[11]
− 30	30	82	0.2	49.3	[12]
− 30	30	66	1	50.9	[14]
− 30	30	326	2.5	70.2	[15]
− 20	68	1053	2	73.1	This work

more advantageous to deicing. Without the reflection of melting water, dry surfaces' absorption performance and photothermal conversion are also better than those of wet surfaces. The contact force between the ice and the superhydrophobic surface is weak [70, 71], making the ice on $fSiO_2$/Mxene@Au-WPU coatings easily removed. The superhydrophobic effect provides a good guarantee for the composite films' photothermal conversion and deicing.

The photothermal deicing efficiency was calculated according to the equation [15, 16]:

$$\eta = \frac{C \cdot \rho \cdot V \cdot \Delta T}{P \cdot t}$$

where C represents the specific heat capacity of ice (2100 J kg^{-1} $°C^{-1}$), ρ represents the density of ice (0.92 g cm^{-3}), V is the volume of ice, P is the power of the NIR laser, and t is the time of photothermal deicing. ΔT is the irradiation area's temperature difference (48.9 °C) before and after the photothermal deicing process. The calculated photothermal deicing efficiency of the $fSiO_2$/MXene@Au-WPU coating was 73.1%, higher than the previous reports in Table 1. Therefore, the $fSiO_2$/MXene@Au-WPU composite presented in this work is a very promising coating material for defrosting and deicing applications.

4 Conclusion

In summary, a new strategy for photothermal deicing employing superhydrophobic plasmonic MXene composites was proposed. The $fSiO_2$/MXene@Au-WPU prepared by a simple spray method achieves high photothermal conversion, superhydrophobicity, and acid (base) resistance. Compared with previous reports, the superhydrophobic coating we prepared featured an ultra-long anti-icing time in a tough environment with low temperature and high humidity (− 20 °C, RH 68%). The composite coatings' high photothermal properties allow for the rapid melting of ice in the irradiated area. The superhydrophobic properties of the coating help melt water slide to the edge. Benefit from these advantages, the coating achieved a deicing efficiency of 73.1%, higher than the existing reports. The spray coating method we used is high throughput, low waste, and can be implemented on many substrates, which is attractive for industrial processes. We believe that if some good methods for improving durability are combined with the as-prepared MXene composites, aging-resistant and mechanically stable superhydrophobic MXene composite coatings will be achieved. Therefore, the composite coating we prepared is expected to have important applications in the efficient anti-icing of outdoor electronic equipment, the anti-corrosion of superhydrophobic special coating, and industrial large-scale film making.

Supplementary Information The online version contains supplementary material available at https://doi.org/10.1007/s42114-022-00549-5.

Funding The authors acknowledge the National Key Research and Development Program of China (2019YFB2203400), the National Natural Science Foundation of China (No. 62075034), and the "111 Project" (B20030). PY acknowledges the National Natural Science Foundation of China (No.62005037). TL wishes to acknowledge the National Department of Science and Education of China (QNJ2021167003) and the Ministry of Science and Technology of China (QN20200023002). DL acknowledges the grant ARC Research Hub for Graphene Enabled Industry Transformation (IH150100003).

Declarations

Conflict of interest The authors declare no competing interests.

References

1. Golovin K et al (2019) Low-interfacial toughness materials for effective large-scale deicing. Science 364:371–375
2. Xie T et al (2016) Experiment investigation on deicing characteristics and energy efficiency using infrared ray as heat source. Energy 116:998–1005
3. Dash S, de Ruiter J, Varanasi KK (2018) Photothermal trap utilizing solar illumination for ice mitigation. Sci Adv 4:eaat0127
4. Wang YD et al (2021) An Online Thermal Deicing Method for Urban Rail Transit Catenary. IEEE T Transp Electr 7:870–882
5. Zhuo YZ et al (2020) Anti-icing ionogel surfaces: inhibiting ice nucleation, growth, and adhesion. ACS Mater Lett 2:616–623

6. Li B et al (2019) Influences of key factors in hot-air deicing for live substation equipment. Cold Reg Sci Technol 160:89–96
7. Wu S et al (2020) Superhydrophobic photothermal icephobic surfaces based on candle soot. P Natl Acad Sci 117:11240–11246
8. Nine MJ et al (2017) Facile adhesion-tuning of superhydrophobic surfaces between "lotus" and "petal" effect and their influence on icing and deicing properties. ACS Appl Mater Inter 9:8393–8402
9. Wang T et al (2016) Passive anti-icing and active deicing films. ACS Appl Mater Inter 8:14169–14173
10. Wang B et al (2022) Ultra-flexible photothermal superhydrophobic coating with multifunctional applications based on plasmonic TiN nanoparticles. Adv Opt Mater 2200168
11. Wang B et al (2022) Upcycling of biomass waste into photothermal superhydrophobic coating for efficient anti-icing and deicing. Mater Today Phys 24:100683
12. Ma L et al (2019) Plasmon-mediated photothermal and superhydrophobic TiN-PTFE film for anti-icing/deicing applications. Compos Sci Technol 181:107696
13. Xie H et al (2021) Efficient and economical approach for flexible photothermal icephobic copper mesh with robust superhydrophobicity and active deicing property. Soft Matter 17:1901–1911
14. Zhang F et al (2021) A durable and photothermal superhydrophobic coating with entwinned CNTs-SiO_2 hybrids for anti-icing applications. Chem Eng J 423:130238
15. Jiang G et al (2018) Superhydrophobic SiC/CNTs coatings with photothermal deicing and passive anti-icing properties. ACS Appl Mater Inter 10:36505–36511
16. Hu JH, Jiang G (2020) Superhydrophobic coatings on iodine doped substrate with photothermal deicing and passive anti-icing properties. Surf Coat Tech 402:126342
17. Liu K et al (2022) Multifunctional slippery polydimethylsiloxane/carbon nanotube composite strain sensor with excellent liquid repellence and anti-icing/deicing performance. Polymers 14:409
18. Li E et al (2021) Asymmetric superhydrophobic textiles for electromagnetic interference shielding, photothermal conversion, and solar water evaporation. ACS Appl Mater Inter 13:28996–29007
19. Weng DH et al (2018) Bioinspired photothermal conversion coatings with self-healing superhydrophobicity for efficient solar steam generation. J Mater Chem A 6:24441–24451
20. Zhang L et al (2021) Functional and versatile superhydrophobic coatings via stoichiometric silanization. Nat Commun 12:982
21. Mazzon G et al (2019) Hydrophobic treatment of woven cotton fabrics with polyurethane modified aminosilicone emulsions. Appl Surf Sci 490:331–342
22. Zhao X et al (2019) Environmentally benign and durable superhydrophobic coatings based on SiO_2 nanoparticles and silanes. J Colloid Interf Sci 542:8–14
23. Zhang Y et al (2023) Influence of mass ratio and calcination temperature on physical and photoelectrochemical properties of ZnFe-layered double oxide/cobalt oxide heterojunction semiconductor for dye degradation applications. Particuology 74:141–155
24. Jing C et al (2022) In-situ constructing visible light CdS/Cd-MOF photocatalyst with enhanced photodegradation of methylene blue. Particuology 69:111–122
25. Ma C et al (2021) Chiral optofluidics with a plasmonic metasurface using the photothermal effect. ACS Nano 15:16357–16367
26. Wang W et al (2021) Broadband thin-film and metamaterial absorbers using refractory vanadium nitride and their thermal stability. Opt Express 29:33456–33466
27. Wang J et al (2020) Broadband Tamm plasmon-enhanced planar hot-electron photodetector. Nanoscale 12:23945–23952
28. Ashalley E et al (2021) Recent progress in chiral absorptive metamaterials. J Elec Sci Tech 19:100098
29. Lin H et al (2017) Two-dimensional ultrathin MXene ceramic nanosheets for photothermal conversion. Nano Lett 17:384–391
30. Liu GY et al (2017) Surface modified Ti_3C_2 MXene nanosheets for tumor targeting photothermal/photodynamic/chemo synergistic therapy. ACS Appl Mater Inter 9:40077–40086
31. Xu DX et al (2020) Insights into the photothermal conversion of 2D MXene nanomaterials: synthesis, mechanism, and applications. Adv Funct Mater 30:2000712
32. Wu H et al (2022) Negative permittivity behavior in flexible carbon nanofibers-polydimethylsiloxane films. Engineered Science 17:113–120
33. Zhang Z et al (2022) Flexible polystyrene/graphene composites with epsilon-near-zero properties. Adv Compos Hybrid Mater 5:1054–1066
34. Xie P et al (2019) Targeted double negative properties in silver/silica random metamaterials by precise control of microstructures. Research 2019:1021368
35. Xie P et al (2022) Recent advances in radio-frequency negative dielectric metamaterials by designing heterogeneous composites. Adv Compos Hybrid Mater 5:679–695
36. Liu J et al (2022) Additive manufacturing of Ti_3C_2-MXene-functionalized conductive polymer hydrogels for electromagnetic-interference shielding. Adv Mater 34:2106253
37. Chaudhuri K et al (2018) Highly broadband absorber using plasmonic titanium carbide (MXene). ACS Photonics 5:1115–1122
38. Li R et al (2017) MXene Ti_3C_2: an effective 2D light-to-heat conversion material. ACS Nano 11:3752–3759
39. Tang WT et al (2019) Multifunctional two-dimensional core-shell MXene@gold nanocomposites for enhanced photo-radio combined therapy in the second biological window. ACS Nano 13:284–294
40. Fan XQ et al (2019) Plasmonic $Ti_3C_2T_X$ MXene enables highly efficient photothermal conversion for healable and transparent wearable device. ACS Nano 13:8124–8134
41. Liu CJ et al (2021) Laser triggered exothermic chemical reaction in Au nanoparticle@ Ti_3C_2 MXene membrane: a route toward efficient light to high-temperature pulse conversion. Chem Eng J 420:127672
42. Ghidiu M et al (2014) Conductive two-dimensional titanium carbide 'clay' with high volumetric capacitance. Nature 516:78-U171
43. Alhabeb M et al (2017) Guidelines for synthesis and processing of two-dimensional titanium carbide ($Ti_3C_2T_X$ MXene). Chem Mater 29:7633–7644
44. Ruan QF et al (2014) Growth of monodisperse gold nanospheres with diameters from 20 nm to 220 nm and their core/satellite nanostructures. Adv Opt Mater 2:65–73
45. Wang B et al (2020) Facile preparation of TPE/SiO_2 flexible superhydrophobic composite film with acid corrosion resistance and stretchable recyclability. Mater Today Commun 25:101318
46. Zhao J et al (2015) Super-hydrophobic surfaces of SiO_2-coated SiC nanowires: fabrication, mechanism and ultraviolet-durable super-hydrophobicity. J Colloid Interf Sci 444:33–37
47. Zuo DC et al (2019) Synthesis of sandwich-like structured Sn/SnOx@MXene composite through in-situ growth for highly reversible lithium storage. Nano Energy 62:401–409
48. Qiao H et al (2020) Black phosphorus nanosheets modified with Au nanoparticles as high conductivity and high activity electrocatalyst for oxygen evolution reaction. Adv Energy Mater 10:2002424
49. Ma JH et al (2020) Au nanoparticles decorated mesoporous SiO_2-WO_3 hybrid materials with improved pore connectivity for ultratrace ethanol detection at low operating temperature. Small 16:2004772
50. Jiang XT et al (2018) Broadband nonlinear photonics in few-layer MXene Ti_3C_2Tx (T = F, O, or OH). Laser Photonics Rev 12:1700229
51. Lipatov A et al (2016) Effect of synthesis on quality, electronic properties and environmental stability of individual monolayer Ti_3C_2 MXene flakes. Adv Energy Mater 2:1600255

52. Zhang JH et al (2020) Au/MoS_2/Ti_3C_2 composite catalyst for efficient photocatalytic hydrogen evolution. Cryst Eng Comm 22:3683–3691
53. Wang J et al (2021) Plasmonic Au nanoparticle@Ti_3C_2Tx heterostructures for improved oxygen evolution performance. Inorg Chem 60:5890–5897
54. Mintcheva N et al (2020) Room-temperature gas sensing of laser-modified anatase TiO_2 decorated with Au nanoparticles. Appl Surf Sci 507:145169
55. Sun Y et al (2021) A signal-on fluorescent aptasensor based on gold nanoparticles for kanamycin detection. RSC Adv 11:10054–10060
56. Štrbac S, Srejić I, Rakočević Z (2018) Electrocatalysis of hydrogen evolution reaction on Au(111) by spontaneously deposited iridium in acid solution. J Electrochem Soc 165:J3335–J3341
57. Li Z et al (2018) Surface nanopore engineering of 2D MXenes for targeted and synergistic multitherapies of hepatocellular carcinoma. Adv Mater 30:1706981
58. Lin H et al (2017) A two-dimensional biodegradable niobium carbide (MXene) for photothermal tumor eradication in NIR-I and NIR-II biowindows. J Am Chem Soc 139:16235–16247
59. Cao W-T et al (2019) MXene-reinforced cellulose nanofibril inks for 3D-printed smart fibres and textiles. Adv Funct Mater 29:1905898
60. Huang X, Wu P (2020) A small amount of delaminated Ti_3C_2 flakes to greatly enhance the thermal conductivity of boron nitride papers by assembling a well-designed interface. Mater Chem Front 4:292–301
61. Pandey RP et al (2018) Ultrahigh-flux and fouling-resistant membranes based on layered silver/MXene (Ti_3C_2Tx) nanosheets. J Mater Chem A 6:3522–3533
62. Stöber W, Fink A, Bohn E (1968) Controlled growth of monodisperse silica spheres in the micron size range. J Colloid Interf Sci 26:62–69
63. Wang S et al (2015) Bioinspired surfaces with superwettability: new insight on theory, design, and applications. Chem Rev 115:8230–8293
64. Daksa Ejeta D et al (2020) Preparation of superhydrophobic and superoleophilic cotton-based material for extremely high flux water-in-oil emulsion separation. Chem Eng J 402:126289
65. Yang J et al (2020) Fabrication of robust and transparent slippery coating with hot water repellency, antifouling property, and corrosion resistance. ACS Appl Mater Inter 12:28645–28654
66. Shao WF et al (2021) Study on favorable comprehensive properties of superhydrophobic coating fabricated by polytetrafluoroethylene doped with graphene. Adv Compos Hybrid Mater 4:521–533
67. Ghadimi MR, Dolati A (2020) Preparation and characterization of superhydrophobic and highly oleophobic FEVE-SiO_2 nanocomposite coatings. Prog Org Coat 138:105388
68. Yousefi E et al (2018) Preparation of new superhydrophobic and highly oleophobic polyurethane coating with enhanced mechanical durability. Appl Surf Sci 454:201–209
69. Long JY et al (2018) Low-cost fabrication of large-area broccoli-like multiscale micro- and nanostructures for metallic superhydrophobic surfaces with ultralow water adhesion and superior anti-frost ability. Adv Mater Interfaces 5:1800353
70. Hou Y, Choy KL (2022) Durable and robust PVDF-HFP/SiO2/CNTs nanocomposites for anti-icing application: water repellency, icing delay, and ice adhesion. Pro Org Coat 163:106637
71. Li Y et al (2022) Solar deicing nanocoatings adaptive to overhead power lines. Adv Funct Mater 32:2113297